

A Deep Learning-Based and Fully Automated Pipeline for Regurgitant Mitral Valve Anatomy Analysis from 3D Echocardiography

Riccardo Munafò^{a,*}, Simone Saitta^a, Giacomo Ingallina^b, Paolo Denti^c,
Francesco Maisano^c, Eustachio Agricola^{b,d}, Alberto Redaelli^a, Emiliano
Votta^a

^a*Department of Electronics, Information and Bioengineering, Politecnico di
Milano, Milan, Italy*

^b*Unit of Cardiovascular Imaging, IRCCS San Raffaele Hospital, Milan, Italy*

^c*Cardiac Surgery Department, IRCCS San Raffaele Hospital, Milan, Italy*

^d*Vita-Salute San Raffaele University, Milan, Italy*

Abstract

Echocardiography, specifically three-dimensional transesophageal echocardiography (3DTEE), is the recommended method for diagnosing mitral regurgitation (MR). 3DTEE provides a high-quality 3D image of the mitral valve (MV), allowing for precise segmentation and measurement of the regurgitant valve anatomy. However, manual TEE segmentations are time-consuming and prone to intra-operator variability, affecting the reliability of the measurements. To address this, we developed a fully automated pipeline using a 3D convolutional neural network (CNN) to segment MV substructures (annulus, anterior leaflet, and posterior leaflet) and quantify MV anatomy. The 3D CNN, based on a multi-decoder residual U-Net architecture, was trained and tested on a dataset comprising 100 3DTEE images with corresponding segmentations from percutaneous MV interventions. Within the pipeline, a custom algorithm refines the CNN-based segmentations and extracts MV models, from which anatomical landmarks and features are quantified. The accuracy of the proposed method was assessed using Dice score and mean surface distance (MSD) against ground truth segmentations, and the extracted anatomical parameters were compared against the semiautomated commercial software TomTec Image Arena. The trained 3D CNN achieved an aver-

*Corresponding Author: riccardo.munafò@polimi.it

age Dice score of 0.79 and MSD of 0.47 mm for the combined segmentation of the annulus, anterior and posterior leaflet. The proposed CNN architecture outperformed a baseline residual U-Net architecture in MV substructure segmentation, and the refinement of the predicted annulus segmentation improved MSD by 8.36%. The annular and leaflet linear measurements differed by less than 7.94 mm and 3.67 mm, respectively, compared to the 3D measurements obtained with TomTec Image Arena. The proposed pipeline was faster than the commercial software, with a modeling time of 12.54 s and a quantification time of 54.42 s. This pipeline improves the MV segmentation and anatomical quantification process, efficiently providing consistent and repeatable results.

Keywords:

Three dimensional transesophageal echocardiography, Mitral regurgitation, Automatic Segmentation, Convolutional Neural Network, Mitral valve anatomy quantification, Mitral Valve

1. Introduction

The mitral valve (MV) consists of two leaflets, named anterior and posterior leaflet, respectively, inserted on a fibrous and muscular ring, called annulus, that is in continuity with the wall of the left ventricle and of the left atrium. The leaflets are connected by fibrous *chordae tendineae* to two papillary muscles that stem from the mid region of the left ventricular wall. In physiologic conditions, during ventricular systole the increase in transvalvular pressure difference drives MV leaflets motion towards the atrium; the synergistic function of all MV substructures allows for leaflet coaptation and MV continence, thus preventing from blood backflow into the atrium. When continence is lost due to the dysfunction of any MV substructure, mitral regurgitation (MR) occurs; if untreated, MR typically worsens and leads to heart failure [8]. The preferred treatment for MR is MV repair, owing to its better short-term results and to significantly better long-term survival rates in the elderly population as compared to MV replacement [7].

Echocardiography is the standard imaging modality in the clinical routine to perform diagnosis of MV regurgitation, according to the guidelines of the European Society of Cardiology (ESC) [23] and the American Heart Association (AHA) [17]. In transesophageal echocardiography (TEE) the ultrasound probe is inserted down the esophagus, resulting in higher-quality images of

the heart due to the proximity to the target structures. TEE allows to acquire two-dimensional (2D) and three-dimensional (3D) images of the heart, 3DTEE being recommended over 2DTEE as it yields more accurate and reproducible volumetric measurements [23, 17]. Clear images of MV can be acquired with the TEE probe at the midesophageal level, a standard view in 3DTEE examinations. Of note, TEE is also used for intraoperative guidance in structural interventional cardiology, i.e., in procedures devoted to treat intracardiac pathologies by implanting *ad hoc* devices by means of a catheter that is inserted at a peripheral access and driven through the bloodstream to the heart [26].

Precise MV segmentation and identification of its substructures (annulus and leaflets) can facilitate accurate and quantitative measurements of the regurgitant MV anatomy to support MR diagnosis, MV repair planning, and intraprocedural maneuvers in structural interventional cardiology. However, manual segmentation of TEE imaging is time-consuming and affected by intra-operator variability that impacts the reliability of the resulting anatomical measurements. In recent years, several works have introduced semi- or fully automatic methods to detect and segment MV structures. Many early methods proposed in the last decade are based on thin tissue detector and active contour algorithms, which require human-in-the-loop-interactions to work properly [3, 22]. In [20], Pouch et al. presented a semi-automatic framework for 4D segmentation and geometric modeling of the MV based on multi-atlas label fusion and template-based medial modeling. Ionasec et al. [11] proposed a fully automatic system for valve modeling, adopting several machine learning algorithms to fit mitral and aortic valve models on both CT [11] and 3DTEE [15, 27] images. Methods based on deep learning, and in particular Convolutional Neural Networks (CNNs), have become increasingly popular for MV segmentation. In [2], Andreassen et al. proposed a mitral annulus segmentation method that leverages 2D CNN-based predictions on individual image slices extracted from a 3DTEE volume to generate a 3D annulus model through an iterative post-processing algorithm. Similarly, Zhang et al. [28] applied a deep reinforcement learning algorithm and a 2D CNN for annulus landmark detection in combination with a spline fitting algorithm to infer the 3D mitral annulus from 3DTEE images. In a recent work, Carnahan et al. [5] proposed a fully automatic method adopting a 3D CNN fed by 3DTEE images for segmentation of MV leaflets in diastole. Overall, previous approaches for MV segmentation from 3DTEE are either time-consuming [3, 22], or semi-automatic [20], or limited in their capability

to capture anatomical variability [11]. On the other hand, the most recent CNN-based methods, which are fully automatic and fast, focus only on the mitral annulus [2, 28] or segment the MV without distinguish among the different substructures [5].

In this paper, we present a fully automated pipeline for MV substructures segmentation and anatomical characterization from 3DTEE. Within our pipeline, a trained 3D CNN is fed by 3DTEE images at end-systole and is able to separately segment the mitral annulus, the anterior leaflet and the posterior leaflet. Leveraging the CNN-based 3D MV model, our pipeline can comprehensively quantify the MV anatomical features relevant to diagnosis, pre-procedural planning or intra-procedural support.

2. Methods

2.1. Data Collection and Manual Segmentation

Intra-procedural 4DTEE acquisitions from 78 candidates to percutaneous MV repair by means of MitraClip system (Abbott) at IRCCS San Raffaele Hospital (Milan, Italy) were collected. Acquisitions were performed using Philips EPIQ CVx scanner with an X8-2T transducer (Philips, Andover, MA, USA). Image data were anonymized and exported in Cartesian format using QLab software (Philips, Andover, MA, USA). The study was approved by the local ethics committee.

Midesophageal views zoomed on the MV were selected from the image data to construct our dataset. Some 4DTEE acquisitions included more than one of these views, which were all considered in our dataset. Acquisitions with serious artifacts were excluded. Our final dataset counted 100 3DTEE volumetric and time-dependent data with a mean voxel spacing of $0.37 \times 0.55 \times 0.24 \text{ mm}^3$ and a mean framerate of 22 per cardiac cycle. For each sequence, the end-systolic frame, identified as the time frame just before aortic valve closure, was selected.

3DTEE data were manually annotated to generate the training and test sets for the 3D CNN. The manual annotations were performed using 3D Slicer [13] by three independent and experienced operators. They segmented different images, ensuring an almost balanced division of the dataset among them. First, each user selected the end systolic frame and placed a series of contour points to define the valve annulus. The contour points were placed at the connections between the leaflets and the myocardium (Fig. 1a, left) on multiple rotating long-axis views and then fitted with a smooth curve

using the Slicer-Heart software [16] (Fig. 1b, left) with a contour radius of 1 mm. The leaflets were sketched manually in multiple parallel long-axis planes that spanned the valve from commissure to commissure (Fig. 1a, right). The selected views in the dataset had the centerline of the volume approximately coinciding with the long axis of the left ventricle. The anterior and posterior leaflets were identified as gray scale pixels with two different labels, between the annulus, defined in the previous step, and the coaptation zone. This resulted in a non-contiguous segmentation of the leaflets on several long-axis slices (Fig. 1b, center), which were then interpolated (Fig. 1b, right) using a morphological contour interpolator filter [1].

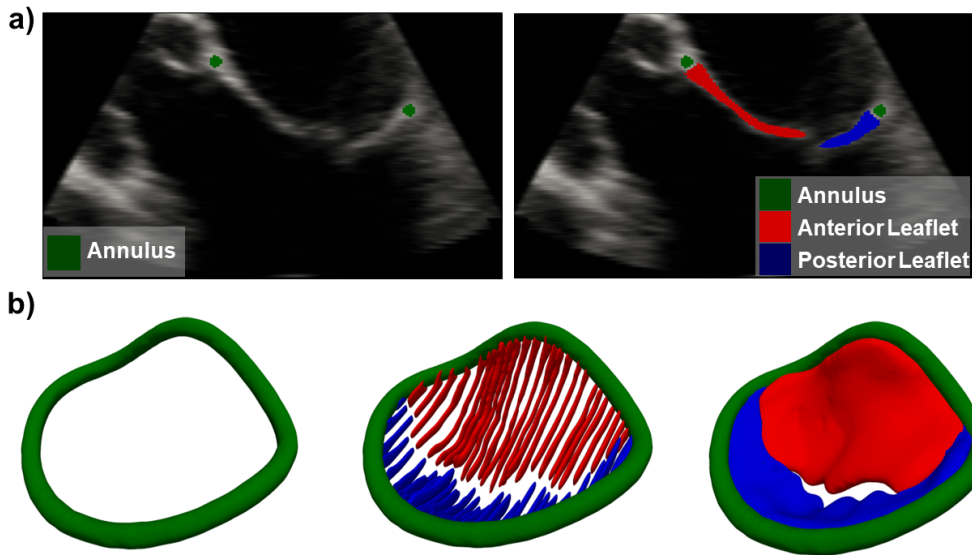


Figure 1: Intermediate and final result of the steps followed to manually annotate 3DTEE images. (a) 3D rendering of the segmentation mask for each step, and (b) corresponding cross sectional view overlapped on the 3DTEE image.

2.2. Neural Network Architecture and Training

The trained CNN was based on a 3D U-Net [21] with encoding and decoding branches of 5 resolution levels each, defined using residual units as shown in [29]. In addition, PReLU activation layers [10] were adopted in each residual unit and the number of decoding branches was extended to three, one for each class detected (i.e., mitral annulus, anterior leaflet and posterior leaflet). This resulted in a multi-decoder version of the residual U-Net.

For the neural network training, 90 volumes (90 %) with ground truth (GT) annotations (training set) were randomly selected. The remaining 10 volumes (10 %) were used as test set to evaluate the performance of the network. A 5-fold cross-validation was performed on the training set. A data augmentation routine was adopted to increase the diversity of the data: transformations taken from the MONAI framework [4] were used including, Gaussian noise, cropping, flipping, rotation and elastic deformation; transformations were applied randomly to the dataset. The model was implemented using the Pytorch framework [18] and it was run on a NVIDIA A100 over 600 epochs with batch size of 3. Novograd optimizer [9] was used with initial learning rate of 0.001, halved every 200 epochs. Intensity of the input images was normalized with values ranging between 0 and 1. A weighted-combination of Dice and Focal losses [25] (with weight of 0.6 and 0.4, respectively) was computed at the output block of each decoder branch. The sum of the loss functions of the three decoders was used to train the neural network.

2.3. Pipeline Implementation

We implemented a fully automatic pipeline (Fig. 2), embedding the trained 3D CNN, for MV segmentation and morphological characterisation. The 3D CNN is fed by 3DTEE images at end-systole and segments the MV by separately recognising the mitral annulus, the anterior leaflet and the posterior leaflet. Given the multi-class segmentation mask provided by 3D CNN (Fig. 2, Segmentation), the implemented pipeline allows to (i) smooth and correct the predicted segmentation (Fig. 2, Refinement), (ii) calculate the position and orientation of the valve, (iii) detect MV anatomical landmarks, (iv) build an approximate model of the coaptation line (Fig. 2, extract MV Features) and (v) quantify MV anatomy (Fig. 2, Quantification of MV Anatomy).

Smoothing and Correction

A marching cubes algorithm [14] is applied to the multi-label segmentation mask to extract three triangulated surface meshes of the mitral annulus Ω_A , and of the anterior Ω_{AL} and posterior leaflet Ω_{PL} , respectively (Fig. 3a and b). The surface meshes are then smoothed using a windowed sinc filter [19]. To correct possible discontinuities in annulus segmentation the skeleton of Ω_A is reconstructed and processed to guarantee a closed profile. Briefly, the valve orifice center \mathbf{x}_c is calculated by taking the average of the coordinates $\mathbf{x}_i = (x_i, y_i, z_i)$ of the n points on Ω_A . Singular-value decomposition

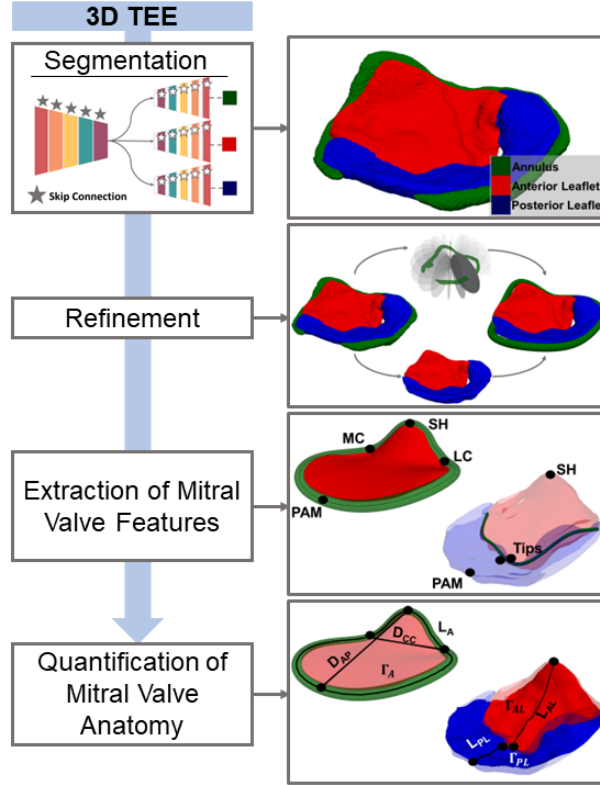


Figure 2: Schematic representation of the implemented automatic pipeline. SH = saddle horn, PAM = posterior annulus mid-point, MC = medial commissure, LC = lateral commissure, D_{CC} = inter-commissural diameter, D_{AP} = antero-posterior diameter, L_A = annulus length, Γ_A = annulus surface, Tips = leaflets tips L_{PL} = posterior leaflet length, L_{AL} = anterior leaflet length, Γ_{AL} = anterior leaflet surface, Γ_{PL} = posterior leaflet surface.

(SVD) on the set of directions $D : \{\mathbf{d}_i = \mathbf{x}_i - \mathbf{x}_c, \quad \mathbf{x}_i \in \Omega_{MA}\}$ allows to define the principal directions of the annulus geometry. The radial \mathbf{r} and normal \mathbf{n} directions are identified through SVD as the direction of highest and lowest variance, respectively. \mathbf{x}_c and \mathbf{n} uniquely identify the plane Π , which is used to define the MV orifice plane in the subsequent steps of the automated pipeline. Multiple-rotating planes are defined around the normal direction \mathbf{n} based on an angular offset ($\theta_{offset} = 15^\circ$). The intersection between these planes and Ω_A identifies a sequence of 3D point sets whose centers of mass outline the mitral annulus shape (Alg. 1). Finally, the skeleton is obtained by interpolating the sequence of centers of mass with a cubic spline. The

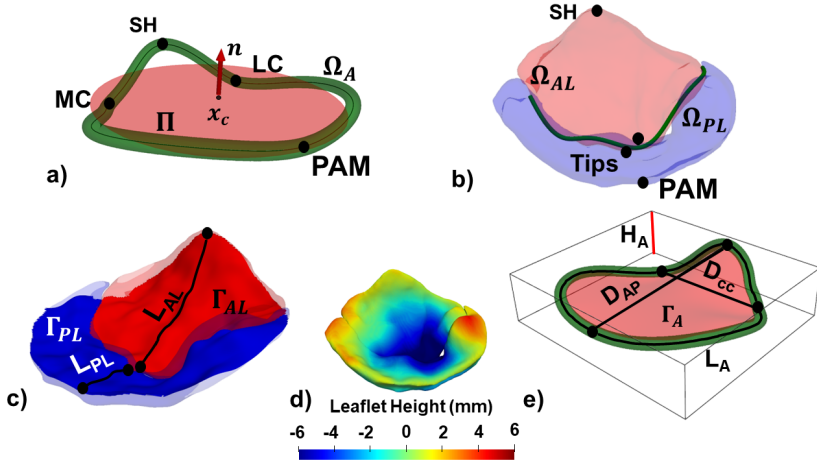


Figure 3: Illustrative example of reconstructed MV model with anatomical features and measurements extracted by the automatic pipeline. (a) Reconstructed and refined mitral annulus (Ω_A) together with the annular anatomical landmarks (SH = saddle horn, PAM = posterior annulus mid-point, MC = medial commissure, LC = lateral commissure), the best fitting plane (Π) and the unitary vector (\mathbf{n}) normal to Π . (b) Reconstructed mitral leaflets (Ω_{AL} =anterior leaflet surface, in red; Ω_{PL} =posterior leaflet surface, in blue), main leaflet landmarks (Tips = leaflets tips), and the reconstructed model of the coaptation line (green). (c) Leaflet 3D middle surfaces (Γ_{AL} , Γ_{PL}) and leaflet 3D measurements (L_{PL} = posterior leaflet length, L_{AL} = anterior leaflet length). (d) Color-coded 3D representation of the reconstructed MV representing leaflet height. (e) 3D surface interpolating the non planar annular profile (Γ_A) and defining the annular area, and annulus 3D measurements (D_{CC} = inter-commissural diameter, D_{AP} = antero-posterior diameter, L_A = annulus length, H_A = annulus height).

skeleton of the annulus is the expanded radially by 1 mm to obtain the corrected version of Ω_A , consistently with the contour radius used for the GT label (Fig. 4).

Detection of Mitral Valve Anatomical Landmarks

The pipeline automatically identifies the MV anatomical landmarks commonly used to describe annulus and leaflet anatomy. This is done using the reconstructed surface meshes Ω_A , Ω_{AL} , and Ω_{PL} .

On the annulus, the saddle horn (SH) and the two commissures (LC, MC) are identified respectively as the highest and the two lowest points of Ω_A skeleton with respect to Π , while the posterior annular midpoint (PAM) is defined as the point opposite to SH in the posterior portion of Γ_A skeleton (Fig. 3a).

Algorithm 1 Definition of skeleton of the mitral annulus from segmentation mask

```

1: Given  $\Omega_A$  and  $D$ 
2:  $\theta_{offset} = 15^\circ$ ,  $\theta = 0^\circ$ 
3:  $\mathbf{n}$  and  $\mathbf{r} \leftarrow \text{SVD}(D)$ 
4: while  $\theta < 2\pi$  do
5:    $\mathbf{r}_\theta \leftarrow \text{Rot}_{\theta_{offset}}(\mathbf{r})$ 
6:    $\Pi \leftarrow \mathbf{n} \times \mathbf{r}_\theta$ 
7:   Find set of intersecting points  $S$  between  $\Pi$  and  $\Omega_A$ 
8:   Compute the center of mass of  $S$ 
9:    $\theta \leftarrow \theta_{offset} + \theta$ 
10: end while

```

On the leaflets, the leaflet tips are identified: a plane ($\Pi_{\text{SH-PAM}}$) passing through SH and PAM and perpendicular to Π is defined; the intersection of this plane with Ω_{AL} and Ω_{PL} identifies two sets of points on the leaflet surface; among these, the leaflet tips (Fig. 3b) are defined as the two points farthest from SH and PAM.

Coaptation Line Identification

The coaptation line is also automatically identified. First, two 3D middle surfaces Γ_{AL} and Γ_{PL} are defined using a 5th order spline radial basis function (RBF) interpolation [24] of Ω_{AL} and Ω_{PL} , respectively. Then, the set of candidate points belonging to the coaptation zone are defined as:

$$P : \{(\mathbf{x}_i, \mathbf{x}_j) \mid \|\mathbf{x}_i - \mathbf{x}_j\| < \epsilon\} \quad (1)$$

with $\mathbf{x}_i \in \Gamma_{\text{AL}}$, $\mathbf{x}_j \in \Gamma_{\text{PL}}$ and ϵ is a specific tolerance set as 0.001 mm. Finally, a least-square fit of point set P with 5th degree polynomial is used to obtain a smooth and continuous line (Fig. 3b).

Quantification of Mitral Valve Anatomy

The final step of the implemented pipeline consists in the automatic computation of MV morphological metrics based on the identified anatomical landmarks. For the annulus, the anterior-posterior diameter (D_{AP}) and the inter-commissural diameter (D_{CC}) are computed as the Euclidian distance from SH to PAM and from MC to LC, respectively. Annular length (L_{A}) is defined as the length of the Ω_{MA} skeleton. Finally, the height of the annulus

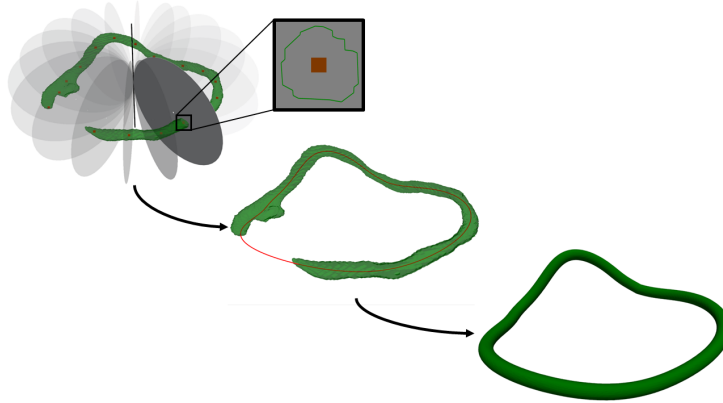


Figure 4: Schematic representation of the three steps for annulus correction, from top left to bottom right. Step one: incomplete annulus mask Ω_A (green) intersected by multiple planes passing through the axis defined by the annulus center and the axis defining the lowest variance of the annular point coordinates; the intersection between a plane and Ω_A is zoomed in, where the corresponding point set defining the cross-sectional profile of Ω_A (green) and their center of mass (red) are depicted. Step two: the centers of mass obtained in step one are interpolated through a cubic spline yielding a complete annulus skeleton (yellow). Step three: the complete skeleton is expanded radially by 1 mm yielding the corrected annulus mask.

(H_A) is defined as the height of the smallest hexahedral bounding box encompassing Ω_{MA} . Also, a 3D surface (Γ_A) representing the non-planar MV orifice is reconstructed using a thin plate radial basis function interpolation [24] of Ω_{MA} . Annular area is defined by as the surface area of Γ_A (Fig. 3e). For the leaflets, the length is defined as the length of the intersection between each leaflet and Π_{SH-PAM} , spanning from the SH to the anterior tip and from PAM to the posterior tip, respectively. Leaflet area is defined as the surface area of Γ_{AL} and Γ_{PL} , respectively (Fig. 3c). The local height of the leaflets is computed as the signed distance of Γ_{AL} and Γ_{PL} , respectively, from the 3D orifice surface Γ_A (Fig. 3d). Leaflet flail or prolapse would result in a greater positive distance from Γ_A .

2.4. Performance Evaluation

For each pair of the 5 training-validation splits, we computed Dice score and Mean Surface Distance (MSD, in mm). Given the points \mathbf{p} of a GT surface S and the points \mathbf{p}' of the corresponding inferred segmentation S' , MSD was defined as:

$$MSD = \frac{1}{n_S + n_{S'}} \left(\sum^{n_S} D(\mathbf{p}, S') + \sum^{n_{S'}} D(\mathbf{p}', S) \right) \quad (2)$$

with $D(\mathbf{p}, S') = \min_{\mathbf{p}' \in S'} \|\mathbf{p} - \mathbf{p}'\|$. The Dice score and the MSD were computed individually for each label and for the complete segmentation mask, i.e., for all the three labels considered together, excluding the background. The network with the best performance over the five folds was then evaluated on the test set using the same metrics. The distance errors were recalculated after the smoothing and correction steps of our pipeline.

The best-performing model was selected for use in our pipeline to extract the relevant anatomical features of the mitral valve (MV) and to quantify its anatomy on the test set. The results of the morphological analysis were compared against measurements performed through TomTec Image Arena (TomTec Imaging Systems GmbH, Unterschleissheim, Germany), a commercial software that provides a semi-automated segmentation tool (4D MV Assessment, 4.6) considered to be the gold standard for MV anatomy segmentation and assessment from 3DTEE images.

The performance of our multi-decoder U-Net was compared to a baseline residual U-Net with an equivalent encoder architecture and a single decoder. Both networks were trained on the combined training and validation set (90 volumes) using the same hyperparameters. The Dice score and MSD were calculated on the test set and the segmentation masks provided by the two networks were visually inspected. All performance metrics are expressed as average value and [min, max] range.

3. Results

3.1. Cross Validation Results and Model Selection

We report in Table 1 the average Dice score and MSD computed with respect to the GT segmentations for each pair of the 5 training-validation splits. Models 2 and 3 provided the highest Dice score for the complete segmentation mask (0.79 [0.74, 0.84] and 0.79 [0.75, 0.85], respectively). With model 3, we obtained higher average Dice scores for annulus (0.41 [0.30, 0.59]) and anterior leaflet (0.80 [0.73, 0.87]). Accordingly, model 3 provided lower average MSD errors for annulus (0.85 mm [0.60 mm, 1.23 mm]), anterior leaflet (0.48 mm [0.27 mm, 0.63 mm]), and complete segmentation mask (0.47 mm [0.32 mm, 0.60 mm]). Therefore, model 3 was re-evaluated on the test set and included in our pipeline.

	Annulus		Anterior		Posterior		Complete Mask	
	Dice Score	MSD [mm]	Dice Score	MSD [mm]	Dice Score	MSD [mm]	Dice Score	MSD [mm]
1	0.43	0.92	0.77	0.52	0.67	0.77	0.77	0.48
2	0.35	1.03	0.78	0.55	0.72	0.67	0.79	0.50
3	0.42	0.85	0.80	0.48	0.67	0.76	0.79	0.47
4	0.27	1.28	0.78	0.52	0.68	0.84	0.77	0.56
5	0.43	0.86	0.75	0.69	0.65	0.98	0.76	0.50
Average	0.38 ± 0.07	0.99 ± 0.18	0.78 ± 0.02	0.55 ± 0.08	0.68 ± 0.02	0.80 ± 0.11	0.78 ± 0.01	0.50 ± 0.04

Table 1: Average Dice scores and MSD in mm for each training on the 5 training-validation pairs. Performance metrics on the validation set are reported for mitral annulus (Annulus), anterior leaflet (Anterior), posterior leaflet (Posterior) and for complete segmentation mask (Complete Mask). Average value across the 5 models and standard deviation are given in the last row.

3.2. Test Set Results

Model 3 was used to run inference on a test set consisting of 10 3DTEE volumes. The trained CNN was capable of accurately extracting the MV substructures anatomy (as shown in Fig. 5). The average Dice scores for the annulus, the anterior leaflet, and the posterior leaflet were 0.39 [0.21, 0.54], 0.78 [0.70, 0.84], and 0.67 [0.36, 0.79], respectively. For the complete segmentation mask, the average Dice score was 0.79 [0.71, 0.84]. The average MSD errors for the annulus, the anterior leaflet, and the posterior leaflet were 1.01 mm [0.56 mm, 1.88 mm], 0.53 mm [0.32 mm, 0.80 mm], and 0.80 mm [0.51 mm, 1.48 mm], respectively. For the complete segmentation mask, the average MSD error was 0.47 mm [0.35 mm, 0.73 mm]. Overall, in 8 test volumes out of 10 the mitral valve was successfully segmented, with few cases in which the mitral annulus presented discontinuities (P6 and P7 in Fig. 5). In one case (P4), the CNN segmented the mitral annulus and the posterior leaflet only partially, and only the inferred anterior leaflet looked plausible at visual observation. Only one test volume (P5) showed sub-optimal segmentation of the anterior and posterior leaflets with many mislabeled regions along the coaptation zone, especially in the medial and lateral portion of the valve. (Fig. 5)

The MSD error for the annulus label was recomputed after applying the correction algorithm for all ten volumes, yielding an average value of 0.93 mm [0.54 mm, 1.85 mm] ($\Delta=-8.36\%$). In all ten test volumes, the refinement of the inferred annulus segmentations yielded reasonable annular profiles, also in those cases where the raw annulus segmentation was discontinuous or incomplete, and reduced the surface error (Fig. 6).

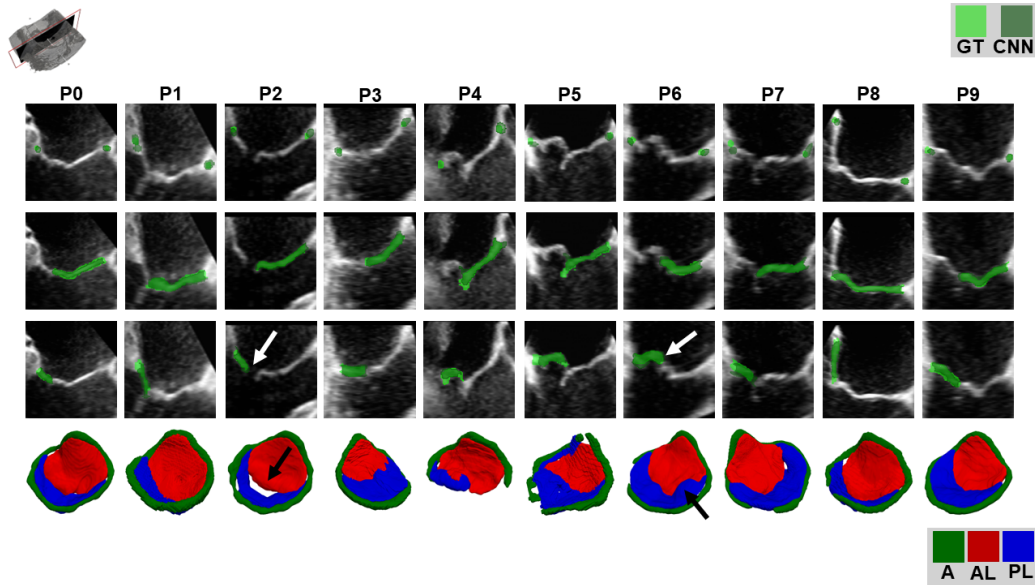


Figure 5: Long-axis views of 3D TEE images and segmentation masks for each volume in test set. In the first 3 rows the GT label is shown in light green, and predicted label (CNN) is shown in dark green for annulus, anterior leaflet and posterior leaflet, respectively. In the fourth row, a 3D representation of predicted segmentation mask is shown, using a color code to distinguish annulus (A), anterior leaflet (AL) and posterior leaflet (PL). White arrows on long-axis views and black arrows on 3D representations highlight leaflet defects (P2) or prolapse (P6) correctly identified in the predicted segmentation masks.

3.3. Comparison vs. Semi-Automated Measurements

The differences between the 3D measurements yielded by the proposed automated pipeline and those obtained by an experienced operator using the semi-automated tool (4D MV Assessment 4.6) embedded in TomTec are detailed in Table 2. For the anatomy of the leaflets, the comparison was carried out upon excluding the two test cases (P4 and P5) the trained 3D CNN failed to segment for at least one leaflet. Overall, a good agreement was found when considering length measurements, although dimensions as estimated by TomTec were larger as compared to those estimated by our approach. The bias was within 7.94 mm for annular measurements and within 3.67 mm for leaflet measurements. The highest bias (250.23 mm²) was found for annulus area estimation. The commercial software required a significant user interaction; for an experienced user, it took around 3 minutes on average to process a single 3DTEE volume.

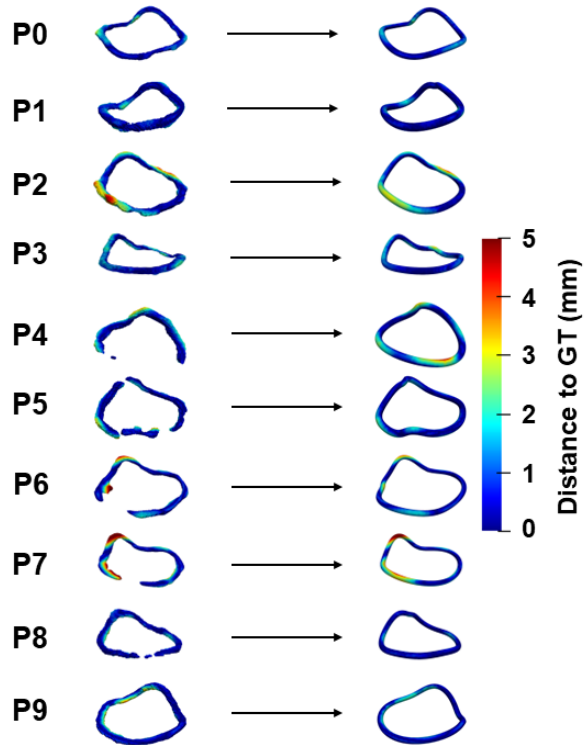


Figure 6: Heatmaps of the distance of the annulus from the GT reference for the 10 patients of the testing set. Data are reported for the annulus before (left column) and after (right column) the smoothing and correction step of our pipeline.

3.4. Comparison with Baseline Residual U-Net

Our proposed Multi-Decoder U-Net architecture outperformed a baseline residual U-Net in terms of segmentation mask quality. This is clearly exemplified in Fig. 7, where the reconstruction for one MV is depicted for both architectures: the baseline residual U-Net identified an annulus with noisy boundaries and with unreasonable tracts at the insertion of the central posterior cusp. The annular region identified by our Multi-Decoder U-Net was not affected by these issues, although it was incomplete in some short tracts; this specific issue was however solved by the subsequent smoothing and correction step of our automated pipeline. The improved quality of the masks yielded by our Multi-Decoder U-Net reflected into the improved average Dice score and MSD errors computed on the test set as compared to those

	Automated pipeline	TOMTEC	Bias	95% limits of agreement
Annulus				
Inter-commisural diameter, mm	36.24	43.79	7.55	[-2.96, 18.07]
Anteroposterior diameter, mm	39.78	42.64	2.86	[-5.68, 11.40]
Height, mm	10.37	10.97	0.60	[-3.68, 4.88]
Length, mm	136.79	144.73	7.94	[-8.53, 24.41]
Area, mm ²	1333.87	1584.10	250.23	[-190.66, 691.12]
Leaflet				
Anterior leaflet length, mm	32.60	35.40	2.79	[-6.12, 11.70]
Posterior leaflet length, mm	14.33	18.00	3.67	[-4.96, 12.30]
Anterior leaflet surface area, mm ²	1057.76	1151.37	93.61	[-283.35, 470.58]
Posterior leaflet surface area, mm ²	768.18	832.87	64.96	[-325.74, 455.13]

Table 2: 3D MV morphology analysis. Comparison between measurements on test set of annulus and leaflet geometry obtained with our automated pipeline and TOMTEC. Mean differences (Bias) and 95% limits of agreement are reported.

obtained with the baseline residual U-Net, especially when considering the three masks, i.e., annulus, anterior leaflet, and posterior leaflet, separately (Table 3).

	Baseline U-Net		Multi-Decoder U-Net	
	Dice Score	MSD [mm]	Dice Score	MSD [mm]
Annulus	0.29 [0.16, 0.38]	1.69 [0.72, 3.42]	0.38 [0.21, 0.53]	1.45 [1.07, 2.84]
Anterior	0.75 [0.67, 0.82]	0.67 [0.45, 1.09]	0.78 [0.63, 0.83]	0.58 [0.40, 1.30]
Posterior	0.58 [0.33, 0.76]	2.02 [0.51, 10.92]	0.63 [0.16, 0.77]	0.97 [0.58, 1.50]
Complete Mask	0.77 [0.68, 0.81]	0.57 [0.45, 0.77]	0.79 [0.71, 0.85]	0.50 [0.45, 0.77]

Table 3: Dice score and MSD errors in mm computed on test set using the baseline Residual U-Net and the multi-decoder Residual U-Net. Data are expressed as mean value and [min, max] range.

3.5. Inference Time

The inference speed required for 3DTEE image segmentation and MV anatomical features extraction was evaluated on the test set. The trained 3D CNN takes on average 0.05 s [0.026 s, 0.22 s] to provide a raw multi-label segmentation mask running on a GPU Nvidia RTX A4000. The automated pipeline took on average 66.98 s [51.39 s, 94.22 s] to perform inference on the complete process using exclusively CPU (Intel Xenon W-2235). Specifically, 12.54 s [7.98 s, 25.42 s] are required on average for MV model refinement, 52.58 s [40.40 s, 68.07 s] for the extraction of anatomical landmarks and features and 1.84 s [0.59 s, 3.24 s] for quantification of MV anatomy. Overall, the proposed pipeline took one third of the time required by an experienced

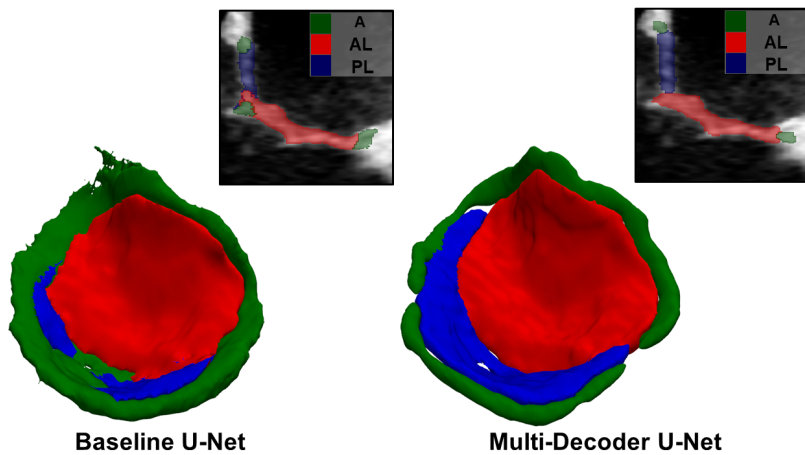


Figure 7: Illustrative example of CNN-based segmentation mask using a baseline U-Net and a Multi-Decoder U-Net. A color-coded 3D rendering of the segmentation mask and a corresponding cross-sectional view overlapped on the 3DTEE image are shown.

user with TomTec Image Arena software to perform MV segmentation and quantitative morphological analysis.

4. Discussion

We presented a deep learning-based pipeline to automatically segment MV substructures (annulus and leaflets) in end-systolic configuration from 3DTEE images, and extract the relevant anatomical landmarks and features to quantify MV anatomy. The pipeline is based on a CNN with a multi-decoder residual U-Net architecture which provides multi-structure end-to-end segmentation that does not require any manual input nor parameter fine-tuning, thus ruling out any dependency on the operator. The trained CNN selected for use in the pipeline achieved an average Dice score of 0.79 (range 0.71-0.85) for the complete segmentation mask, which is comparable to the Dice score (0.81 ± 0.07) reported in [5]. However, Carnahan et al. [5] trained a 3D CNN to automatically segment the MV in its entirety without distinguishing its substructures. Moreover, they reconstructed the anatomy of the MV leaflets in its open configuration; that choice inherently prevents the identification of the leaflet coaptation line. This anatomical feature is key in supporting the quantitative identification of coaptation defects, and it is a crucial landmark in percutaneous MV repair, where the pose of the

implantable device must be set by the operator accounting for the location of the defect and for the local orientation of the coaptation line. As shown in Fig. 5, the predicted segmentation masks were overall consistent with the corresponding GT segmentations. The mitral annulus is the label that showed the least overlap with the GT datum, as suggested by the low Dice score obtained for this label. However, it should be pointed out that the annulus is the thinnest structure; thus, small discrepancies in annular profile may reflect in a notable decrease in Dice score. On the other hand, the anterior and posterior leaflets showed a good degree of overlap with the corresponding GT segmentations, especially along the coaptation region. This result suggests that our automated pipeline reliably identifies leaflet contact regions, coaptation defects (P2 in Fig. 5) or prolapses (P6 in Fig. 5), which are distinctive features of regurgitant valves candidates to surgical or percutaneous MV repair. Of note, inaccuracies in our automated segmentation were minor. The average surface distance to the GT data for the full segmentation mask was of the order of the spatial resolution of the TEE volumes in our dataset (0.30-0.70 mm/voxel). Furthermore, the reported distance was almost equal to the inter-user variability typical of manual segmentation, previously reported as 0.6 ± 0.17 mm [12], and compared favorably with previous semi-automatic (0.59 ± 0.49 mm [22] and 0.60 ± 0.20 mm [20]) and fully automated methods (1.54 ± 1.17 mm [11] and 0.59 ± 0.23 mm [5]). Average surface errors were slightly lower than surface distance computed for the complete segmentation mask when calculated for each label separately. This worsening of the MSD is mainly related to the lack of intensity-based boundaries for MV structures in the 3DTEE images. The CNN provided poor quality segmentation of the leaflets in one test volume (P5 in Fig. 5) and segmented incompletely the mitral annulus and the posterior leaflet in another test volume (P4 in Fig. 5). For both cases, the low performance can be related to the scarce quality of the TEE data, which were affected by a high speckle noise. Nevertheless, as shown in Fig. 6 the implemented correction algorithm enabled a robust and complete reconstruction of the annulus resulting in a significant improvement of performance metrics. Moreover, based on the average distance error for the predicted annulus (0.93 mm [0.54 mm, 1.85 mm]), the proposed pipeline outperformed the approaches proposed in [28] (2.74 mm) and [2] (2 mm) for mitral annulus segmentation. Furthermore, our proposed multi-decoder residual U-Net architecture outperformed a baseline residual U-Net in segmenting MV from 3DTEE images, as it provided better quality segmentation

masks, especially in identifying the boundaries of MV structures (Fig. 7). This result suggests that the multi-decoder architecture can mitigate the lack of intensity-based boundaries for cardiac structures in ultrasound images that makes it hard to distinguish between the different components of these structures with automatic methods. The multiple decoders allow the network to incorporate information from multiple scales and levels of abstraction, improving its ability to distinguish different structures even in the absence of clear intensity-based boundaries. This makes the multi-decoder U-Net architecture a more effective tool for the automated segmentation of ultrasound images as compared to simpler architectures.

The pipeline also demonstrated consistent identification of MV anatomical landmarks and reconstruction of anatomical features extracted from the CNN-based MV model. Overall, good agreement was found between our proposed method and TomTec Image Arena, with differences in annular and leaflet linear measurements of less than 7.94 mm and 3.67 mm, respectively. The highest bias (250.23 mm^2) was found for annulus area estimation. As a matter of fact, TomTec Image Arena Software overestimated the annular area since it simply identifies the mitral annulus as a closed line representing the outer border of the mitral leaflets identified as single surfaces. Our automated pipeline, on the other hand, represents the mitral annulus and leaflets with thickness, providing a more realistic MV representation. The comparison with commercial software is further proof of the accuracy and robustness of the proposed segmentation method. To the best of our knowledge, only the very recent work by Chen et al. [6] tested a CNN-based method for MV segmentation against commercial software. However, their comparison was limited to the annulus, and their results were similar to our own findings. It is worth noting that Chen et al. used a larger dataset, consisting of twenty-eight 3D volumes, to evaluate the accuracy of their approach, while our study only used ten 3D volumes.

Finally, the proposed pipeline is fully automated and requires no manual input at any of its steps. The resulting segmentations and subsequent analyses will therefore be more reproducible than those yielded by manual or semi-automated approaches. The proposed pipeline provided a full and refined MV model in 12.54 s on average (range [7.98 s, 25.42 s]); hence, it proved substantially faster than the gold standard method herein considered for comparison, which also required extensive user interaction.

To the best of our knowledge, none of the previously proposed methods for MV segmentation integrated annulus and leaflets quantitative characterisa-

tion into a single workflow like the pipeline presented here. As compared to previous CNN-based approaches for segmentation of TEE images that focused only on mitral annulus [28, 2] or leaflets segmentation [5], our trained 3D CNN proved capable of segmenting and identifying all substructures of the MV. Moreover, our approach addressed the challenging task of segmenting regurgitant MVs at end-systole. The characterization of annulus and leaflets anatomy at this time instant allows to extract relevant information to support MR diagnosis and MV repair planning.

4.1. Limitations and Future work

Our trained 3D CNN provided sub-optimal MV substructures segmentations in two test images out of ten. As previously pointed out, this failure can be attributed to the low image quality and speckle noise that affected these images. Excluding images affected by this type of noise from the dataset would certainly ensure better performance in the quality of MV structure segmentation. However, such a dataset would not be consistent with real world applications, where the above mentioned noise is inherent to ultrasound images and cannot be avoided during acquisitions. Future efforts will have to be devoted to include a wider variation in image quality by expanding our data set. Extending the method to a temporal segmentation problem could also help increasing its accuracy, as well as provide a comprehensive assessment of MV anatomy over the entire cardiac cycle. In fact, some MV substructures (e.g., the leaflets) are better imaged at specific phases of the cardiac cycle. By enforcing the anatomical continuity of segmented MV structures in each frame during 3D CNN training, we could improve our results and overcome limitations due to image quality. Finally, as all CNN-based segmentation methods, our pipeline would be in principle well suited for intraoperative use in percutaneous MV repair. Indeed, the automatic localization of the coaptation line and the quantification of valve orientation would visualization of the target defects and hence facilitate optimal catheter positioning before the actual device deployment. However, the time required by the proposed pipeline to extract MV characteristics is still not compatible with real-time applications. Further work is needed to overcome this limitations and may include the exploitation of GPU support throughout the entire workflow.

5. Conclusion

We presented a fully automated, 3D CNN-based pipeline for MV segmentation from 3DTEE and identification of anatomical landmarks and relevant features in regurgitant MVs. The designed pipeline improves the workflow for MV segmentation and anatomical quantification of the mitral annulus and leaflets, providing consistent and repeatable results in a comprehensive and fast way. This pipeline will potentially lead to a more reproducible and time-efficient quantification of MV anatomy to support the diagnosis of MR and planning of MV repair, with a potential future extension to intraoperative support in transcatheter MV repair surgeries.

Acknowledgements

This work has received funding from the European Union's Horizon 2020 research and innovation programme under grant agreement No. 101017140, the ARTERY project.

References

- [1] Albu, A.B., Beugeling, T., Laurendeau, D., 2008. A morphology-based approach for interslice interpolation of anatomical slices from volumetric images. *IEEE Transactions on Biomedical Engineering* 55, 2022–2038.
- [2] Andreassen, B.S., Veronesi, F., Gerard, O., Solberg, A.H.S., Samset, E., 2019. Mitral annulus segmentation using deep learning in 3-d transesophageal echocardiography. *IEEE journal of biomedical and health informatics* 24, 994–1003.
- [3] Burlina, P., Sprouse, C., DeMenthon, D., Jorstad, A., Juang, R., Contijoch, F., Abraham, T., Yuh, D., McVeigh, E., 2010. Patient-specific modeling and analysis of the mitral valve using 3d-tee, in: *International Conference on Information Processing in Computer-Assisted Interventions*, Springer. pp. 135–146.
- [4] Cardoso, M.J., Li, W., Brown, R., Ma, N., Kerfoot, E., Wang, Y., Murrey, B., Myronenko, A., Zhao, C., Yang, D., et al., 2022. Monai: An open-source framework for deep learning in healthcare. *arXiv preprint arXiv:2211.02701* .
- [5] Carnahan, P., Moore, J., Bainbridge, D., Eskandari, M., Chen, E., Peters, T.M., 2021. Deepmitral: Fully automatic 3d echocardiography segmentation for patient specific mitral valve modelling, in: *International Conference on Medical Image Computing and Computer-Assisted Intervention*, Springer. pp. 459–468.
- [6] Chen, J., Li, H., He, G., Yao, F., Lai, L., Yao, J., Xie, L., 2023. Automatic 3d mitral valve leaflet segmentation and validation of quantitative measurement. *Biomedical Signal Processing and Control* 79, 104166.
- [7] Di Tommaso, E., Rapetto, F., Guida, G.A., Zakkar, M., Bruno, V.D., 2021. Benefits of mitral valve repair over replacement in the elderly: a systematic review and meta-analysis. *Journal of Cardiac Surgery* 36, 2524–2530.
- [8] El Sabbagh, A., Reddy, Y.N., Nishimura, R.A., 2018. Mitral valve regurgitation in the contemporary era: insights into diagnosis, management, and future directions. *JACC: Cardiovascular Imaging* 11, 628–643.

- [9] Ginsburg, B., Castonguay, P., Hrinchuk, O., Kuchaiev, O., Lavrukhin, V., Leary, R., Li, J., Nguyen, H., Zhang, Y., Cohen, J.M., 2019. Stochastic gradient methods with layer-wise adaptive moments for training of deep networks. arXiv preprint arXiv:1905.11286 .
- [10] He, K., Zhang, X., Ren, S., Sun, J., 2015. Delving deep into rectifiers: Surpassing human-level performance on imagenet classification, in: Proceedings of the IEEE international conference on computer vision, pp. 1026–1034.
- [11] Ionasec, R.I., Voigt, I., Georgescu, B., Wang, Y., Houle, H., Vega-Higuera, F., Navab, N., Comaniciu, D., 2010. Patient-specific modeling and quantification of the aortic and mitral valves from 4-d cardiac ct and tee. IEEE transactions on medical imaging 29, 1636–1651.
- [12] Jassar, A.S., Brinster, C.J., Vergnat, M., Robb, J.D., Eperjesi, T.J., Pouch, A.M., Cheung, A.T., Weiss, S.J., Acker, M.A., Gorman III, J.H., et al., 2011. Quantitative mitral valve modeling using real-time three-dimensional echocardiography: technique and repeatability. The Annals of thoracic surgery 91, 165–171.
- [13] Kikinis, R., Pieper, S.D., Vosburgh, K.G., 2014. 3d slicer: a platform for subject-specific image analysis, visualization, and clinical support, in: Intraoperative imaging and image-guided therapy. Springer, pp. 277–289.
- [14] Lorensen, W.E., Cline, H.E., 1987. Marching cubes: A high resolution 3d surface construction algorithm. ACM siggraph computer graphics 21, 163–169.
- [15] Mansi, T., Voigt, I., Georgescu, B., Zheng, X., Mengue, E.A., Hackl, M., Ionasec, R.I., Noack, T., Seeburger, J., Comaniciu, D., 2012. An integrated framework for finite-element modeling of mitral valve biomechanics from medical images: application to mitralclip intervention planning. Medical image analysis 16, 1330–1346.
- [16] Nguyen, A.V., Lasso, A., Nam, H.H., Faerber, J., Aly, A.H., Pouch, A.M., Scanlan, A.B., McGowan, F.X., Mercer-Rosa, L., Cohen, M.S., et al., 2019. Dynamic three-dimensional geometry of the tricuspid valve

annulus in hypoplastic left heart syndrome with a fontan circulation. *Journal of the American Society of Echocardiography* 32, 655–666.

- [17] Otto, C.M., Nishimura, R.A., Bonow, R.O., Carabello, B.A., Erwin III, J.P., Gentile, F., Jneid, H., Krieger, E.V., Mack, M., McLeod, C., et al., 2021. 2020 acc/aha guideline for the management of patients with valvular heart disease: executive summary: a report of the american college of cardiology/american heart association joint committee on clinical practice guidelines. *Journal of the American College of Cardiology* 77, 450–500.
- [18] Paszke, A., Gross, S., Massa, F., Lerer, A., Bradbury, J., Chanan, G., Killeen, T., Lin, Z., Gimelshein, N., Antiga, L., Desmaison, A., Kopf, A., Yang, E., DeVito, Z., Raison, M., Tejani, A., Chilamkurthy, S., Steiner, B., Fang, L., Bai, J., Chintala, S., 2019. Pytorch: An imperative style, high-performance deep learning library, in: Wallach, H., Larochelle, H., Beygelzimer, A., d'Alché-Buc, F., Fox, E., Garnett, R. (Eds.), *Advances in Neural Information Processing Systems* 32. Curran Associates, Inc., pp. 8024–8035.
- [19] Pinter, C., Lasso, A., Fichtinger, G., 2019. Polymorph segmentation representation for medical image computing. *Computer methods and programs in biomedicine* 171, 19–26.
- [20] Pouch, A.M., Aly, A.H., Lai, E.K., Yushkevich, N., Stoffers, R.H., Gorman, J.H., Cheung, A.T., Gorman, R.C., Yushkevich, P.A., 2017. Spatiotemporal segmentation and modeling of the mitral valve in real-time 3d echocardiographic images, in: *International Conference on Medical Image Computing and Computer-Assisted Intervention*, Springer. pp. 746–754.
- [21] Ronneberger, O., Fischer, P., Brox, T., 2015. U-net: Convolutional networks for biomedical image segmentation, in: *International Conference on Medical image computing and computer-assisted intervention*, Springer. pp. 234–241.
- [22] Schneider, R.J., Tenenholtz, N.A., Perrin, D.P., Marx, G.R., Nido, P.J.d., Howe, R.D., 2011. Patient-specific mitral leaflet segmentation from 4d ultrasound, in: *International Conference on Medical Image Computing and Computer-Assisted Intervention*, Springer. pp. 520–527.

- [23] Vahanian, A., Beyersdorf, F., Praz, F., Milojevic, M., Baldus, S., Bauersachs, J., Capodanno, D., Conradi, L., De Bonis, M., De Paulis, R., et al., 2022. 2021 esc/eacts guidelines for the management of valvular heart disease: developed by the task force for the management of valvular heart disease of the european society of cardiology (esc) and the european association for cardio-thoracic surgery (eacts). *European heart journal* 43, 561–632.
- [24] Wright, G.B., 2003. Radial basis function interpolation: numerical and analytical developments. University of Colorado at Boulder.
- [25] Yeung, M., Sala, E., Schönlieb, C.B., Rundo, L., 2022. Unified focal loss: Generalising dice and cross entropy-based losses to handle class imbalanced medical image segmentation. *Computerized Medical Imaging and Graphics* 95, 102026.
- [26] Zamorano, J.L., Badano, L.P., Bruce, C., Chan, K.L., Gonçalves, A., Hahn, R.T., Keane, M.G., La Canna, G., Monaghan, M.J., Nihoyannopoulos, P., et al., 2011. Eae/ase recommendations for the use of echocardiography in new transcatheter interventions for valvular heart disease. *European heart journal* 32, 2189–2214.
- [27] Zhang, F., Kanik, J., Mansi, T., Voigt, I., Sharma, P., Ionasec, R.I., Subrahmanyam, L., Lin, B.A., Sugeng, L., Yuh, D., et al., 2017. Towards patient-specific modeling of mitral valve repair: 3d transesophageal echocardiography-derived parameter estimation. *Medical image analysis* 35, 599–609.
- [28] Zhang, Y., Amadou, A.a., Voigt, I., Mihalef, V., Houle, H., John, M., Mansi, T., Liao, R., 2020. A bottom-up approach for real-time mitral valve annulus modeling on 3d echo images, in: *International Conference on Medical Image Computing and Computer-Assisted Intervention*, Springer. pp. 458–467.
- [29] Zhang, Z., Liu, Q., Wang, Y., 2018. Road extraction by deep residual u-net. *IEEE Geoscience and Remote Sensing Letters* 15, 749–753.